

Self-propulsion of a light-powered microscopic crystalline flapper in water*Kazuma Obara, Yoshiyuki Kageyama,* and Sadamu Takeda*

((Optional Dedication))

K. Obara

Graduate School of Chemical Sciences and Engineering, Hokkaido University, Sapporo, 060-0810, Japan

Y. Kageyama, S. Takeda

Faculty of Science, Hokkaido University, Sapporo, 060-0810, Japan

E-mail: y.kageyama@sci.hokudai.ac.jp

Keywords: active matter, microrobot, light-driven motor, dissipative self-organization, scallop theorem, symmetry breaking, energy conversion

A key goal in developing molecular microrobots that mimic real-world animal dynamic behavior is to understand better the self-continuous progressive motion resulting from collective molecular transformation. This study reports, for the first time, the experimental realization of directional swimming of a microcrystal that exhibits self-continuous reciprocating motion in a two-dimensional water tank. Although the reciprocal flip motion of the crystals was like that of a fish wagging its tail fin, many of the crystals swam in the opposite direction to which a fish would swim. Here we explore the directionality generation mechanism and physical features of the swimming behavior by constructing a mathematical model for the crystalline flapper. The results show that a tiny crystal with a less-deformable part in its flip fin exhibits a pull-type stroke swimming, while a crystal with a fin that uniformly deforms exhibits push-type kicking motion.

1. Introduction

The development of molecular microrobots with motional dynamics based on the characteristics of living systems has attracted considerable attention from physicists and chemists, and offers enormous potential in applications ranging from intelligent machines to biomedical devices.^[1] The first challenge to overcome to enable progress toward these

potential applications is attaining self-organized macroscopic dynamics in molecular machines. The next challenge is creating directional self-propelling motion that can be regarded as mechanical work created from the self-sustained transformation of a molecular machine. Generally, the motion of an inanimate object is passive: alternation in the environment repetitively drives its movement.^[2] There have been reports of traveling light-induced locomotion of photochromic^[3] or photothermal^[4] materials, as well as other motion in stimuli-responsive materials.^[5] Only objects possessing an ability to convert supplied energy to kinetic energy on a scale larger than thermal fluctuation can move self-sustainably.^[1e, 6] The directions of motion are defined by asymmetries of the object, anisotropies in its surroundings, or both. For example, Janus particles, whose surfaces have two distinct chemical or photocatalytic properties, show self-propulsion in aqueous solutions.^[7] Oil droplets migrate for long periods driven by the spontaneously induced local gradient of surface tension.^[8] An \cap -shaped chemical-oscillatory hydrogel can display walking motions on a structurally-asymmetric substrate,^[9] and some photoresponsive objects showed light-guided directional motion or transportation.^[10] As can be understood from these examples, self-continuous features and spatial asymmetry are required for matter to show dynamic activity.^[11]

Previously, we reported our realization of light-powered self-oscillatory flipping of submillimeter-sized crystals wherein their spatially and temporally self-patterned features were characterized not by the light-source direction but by internal chemical and physical processes.^[12] The crystals were prepared from a synthesized azobenzene derivative (6-[4-(4-butylphenylazo)phenoxy]hexanoic acid, **1**)^[13] and oleic acid (**2**).^[14] The self-repetitive bending-and-flattening motion occurred via crystalline phase transition triggered by photoisomerization. Photoisomerization increases the *cis*-isomer ratio to induce the forward phase transition which bends the outline; the phase transition then switches the efficiency of photoisomerization to reverse the reaction, and the resultant decrease in *cis*-isomer ratio

induces an unbending motion via backward phase transition to the original phase. This powerful autonomous flipping allowed the crystal to exert mechanical force on its surroundings. In the present study, we report the swimming mechanics of tiny self-flipping crystals in a flat-box water pool; in our previous work, we focused on the generation and mechanism of macroscopic self-oscillation^[12] and the investigation of crystalline structure^[15]. In liquids, viscous drag forces act against the motion of small objects.^[1b, 16] This drag causes both a gain in the swimming thrust force as well as a prohibition of the inertial motion of the object. As a result, the object stops immediately upon changing its position. If the deformation of an object is a reciprocal process, the sum of the displacement of the object in a Newtonian fluid (in which fluid inertia is negligible) is zero. This feature is known as the scallop theorem.^[17] How to break this theorem and realize directional motion in a viscous liquid is a fundamental issue to be resolved in the development of mobile microrobots.^[1a]

In theoretical studies, the three-link swimmer model has often been applied in an attempt to break the scallop theorem, because it is the simplest model for an object that shows asymmetric deformation.^[18] According to theoretical modeling studies, the scallop theorem can be violated under conditions in which the reciprocal objects are subject to anisotropic drag. In the present experiments, the crystals displayed reciprocal motion yet showed a net directional movement. This phenomenon suggests that the reciprocal motion was asymmetric on a macroscopic scale. Because the crystals' vertical movement was likely limited by the large drag force due to the flat-box shape of the water pool, we constructed a model for a swimming crystal in which vertical motion was restricted. Through our numerical analysis it was revealed that a slight difference in shape determines the swimming direction of the crystal.

2. Experimental Section

General considerations

All experimental observations were obtained as described in our previous paper.^[12] For the preparation of the co-crystal, a mixture of **1** and sodium salt of **2** was dispersed in phosphate buffered saline (pH 7.5) and ultrasonicated at 55°C for 30 min, then was cooled to room temperature in darkness. The dispersed crystals were placed into the water pool, which was built using two glass slides (Matsunami Glass, Japan) and a 0.3 mm thick plastic frame (Frame Seal, Bio-Rad, USA). The dynamics of the crystal were recorded using a differential interference contrast microscope (Nikon, Ti-U or TE2000, Japan) equipped with an incident fluorescent unit, the light source of which was a high-pressure mercury lamp, and a CCD camera (Omron Sentech, TC152USB-AH or MCE132U3V, Japan). A Plan Fluor ELWD 20× objective lens (NA 0.45, Nikon, Japan) was used for observation of the swimming motion. The excitation wavelength was monochromized using a 435 nm narrow bandpass filter (band width: 10 nm), or colored by a 420–490 nm wide bandpass filter. An illustration of the equipment is shown in Figure S1 in the supporting information. As previously reported,^[12] the duration of the photoisomerization processes (steps 1 and 3) were shifted by the filter types, but the deformation style at steps 2 and 4, displacement per one-round flipping, and direction of the swimming were generally unaffected by filter type. For measuring outlines and tracking movements of the crystals, we used Image-Pro Premier software, versions 9.2 and 9.3 (Media Cybernetics, USA). The elevation angle (θ_{obs}) was estimated from the ratio of the projection-length of the fin before and after bending. For mathematical analyses, Matlab versions 2020b and 2021a (Mathworks, USA) were employed.

Development of the mathematical model

Herein, we set a *three-panels-two-torsion springs* object with 100 μm length, 40 μm width, and 1 μm height as a model to simulate the curved bending of the molecular crystal (Figure 1). In this model, we considered the rotational motions of panel-1 and panel-2 and fixed the vertical position of panel-0. The horizontal component of the drag force to the rotational

motion of the panels is employed as the thrust for the translational motion. The effect of viscous resistance against translation on the fin-rotation was ignored because the estimated resistance has a small value and low accuracy due to the complexity of hydrodynamics. We simulated four types of motion (Figure 1): in Type-A, a single spring alters the equilibrium point as the result of phase transition; in Types B1 and B2, both springs alter the equilibrium point one after the other; in Type-C, both springs alter the equilibrium point simultaneously.

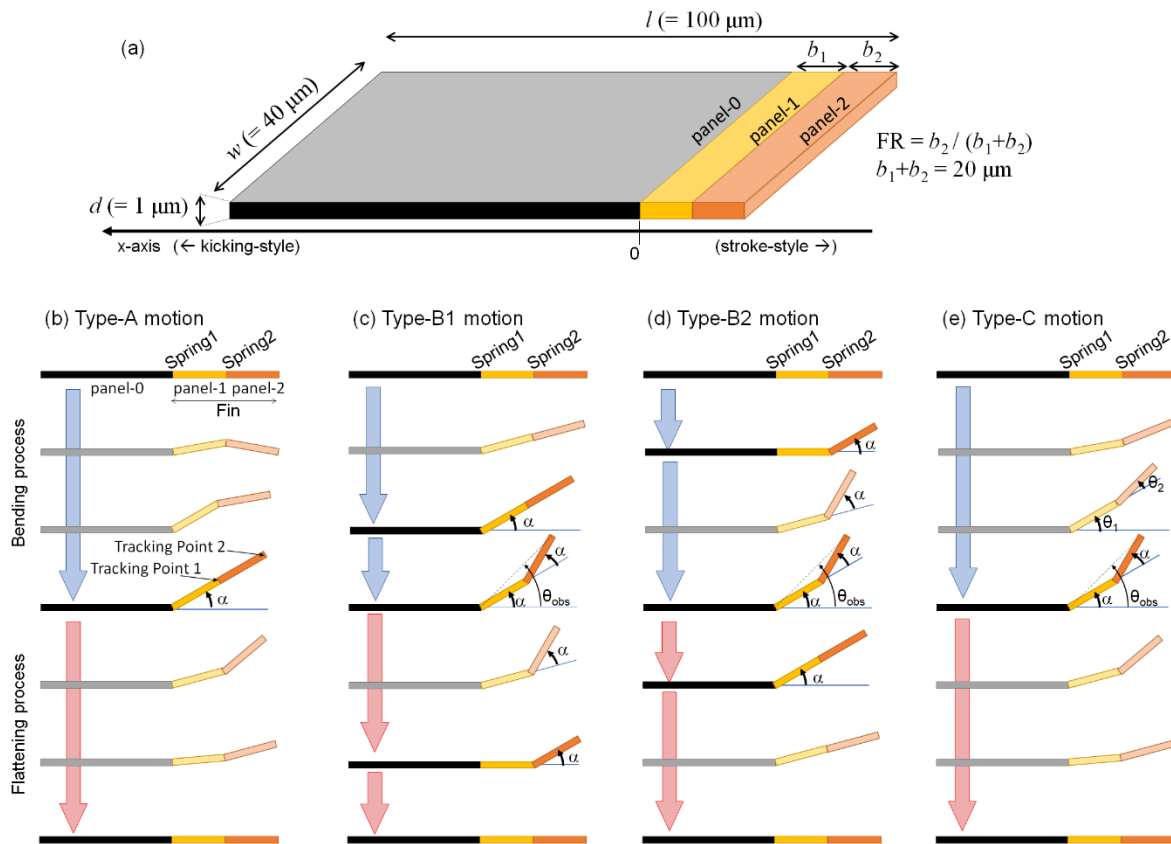


Figure 1. (a) Definition of the shape of the object for the three-panel-two-torsion spring model. (b–d) Definition of the angles and points for tracking dynamics and schematic illustration to show the orders of the panels' motions for mathematical analysis. (b) Type-A motion, where the balanced angle of spring-1 shifts from zero to α to start the bending process, and from α to zero to start the flattening process, while the balanced angle of spring-2, which is act as a spring with same spring constant to that of spring-1, is constant at zero . (c) Type-B1 motion, in which the bending process occurs via the shift of the balanced angle of spring-2 from zero to α , followed by the shift of the balanced angle of spring-1 from zero to α . For the flattening process, the balanced angle of spring-2 shifts from α to zero, and then the balanced angle of spring-1 shifts to zero. The spring opposite to the working-spring is fixed in the model. (d) Type-B2 motion, which is the time-reversal motion of type-B1. (e) Type-C motion, in which the bending process occurs via the simultaneous shift of the balanced angles of both spring-1 and spring-2 from zero to α , and the flattening process occurs via the shift of both springs from α to zero.

The swimming motion can be described by two equations of motion (EOM). The first EOM is for rotation of the panel (Eq.1):

$$I \frac{d^2}{dt^2} \theta = T_s - T_{Drot} \quad (1)$$

Where I is the inertia moment of the rotating panel, θ is the elevation angle of the panel as seen from the next panel on the body side, T_s is the torque working on the panel caused by the torsion spring, and T_{Drot} is the torque derived from the drag force working on the panel while flipping. The second EOM is for translation of the set of panels (Eq. 2):

$$m \frac{d^2}{dt^2} x = Th_{transl} - D_{transl} \quad (2)$$

Where m is the mass of the set of panels, x is the position, Th_{transl} is the thrust for the translation obtained as the drag force for the panel's rotation, and D_{transl} is the drag force working on the set of panels against the translational motion.

For simplicity, we assumed that the drag force (D) was the linear sum of the drag on the cross-section and that on the shear plane (Eq. 3):

$$D = \frac{1}{2} \rho C_d S_d v_{\perp}^2 + \frac{1}{2} \rho C_f S_f v_{\parallel}^2 \quad (3)$$

Where ρ is the mass density of the fluid, C_d and C_f , and S_d and S_f are the drag coefficients and areas for the cross-sectional and side-sectional faces of the object, respectively, and v_{\perp} and v_{\parallel} are the speeds of the object perpendicular to and parallel to the rotation direction, respectively. According to Azuma^[19], C_d and C_f for rectangular objects with low Reynolds number dynamics were reported as $(10.9/Re) / (0.96 - \log Re)$, and $(4 \pi / Re) / (3.2 - 2.3 \log Re)$, respectively; to calculate the Reynolds number, $Re = v L / \nu$, ν is the kinematic viscosity of the fluid, L is characteristic length, and v is velocity of the object. Therefore, in our numerical analysis for the object with 40 μm characteristic length, we employ Z_d/Re ($Z_d = 8$) as C_d for rotation, Z_d'/Re ($Z_d' = 2$) as C_d for translation, and Z_f/Re ($Z_f = 1$) as C_f , because the means of angular velocities and translation velocity were expected to be 10^2 rad/s ($Re = 10^{-1} \sim 10^0$) and

$10^1 \mu\text{m/sec}$ ($\text{Re} = 10^{-4} \sim 10^{-3}$), respectively. In addition, we regarded the densities of the fluid (ρ) and the object as 10^3 kg/m^3 and the kinematic viscosity of the fluid (ν) as $10^{-6} \text{ m}^2/\text{s}$. We did not consider any additional mass in the model.

Next, we built EOM for the rotary motion of each panel.

EOM of panel 2 is presented using maximal elevation angle (α_2) as:

$$I = \frac{1}{3} m_2 b_2^2 \quad (4)$$

$$T_s = -k_2(\theta_2 - \alpha_2) \quad \text{for outbound step (bending step)} \quad (5)$$

$$T_s = -k_2(-\theta_2) \quad \text{for inbound step (flattening step)} \quad (6)$$

$$T_{Drot} = \frac{1}{2} \rho \nu Z_d \left(\frac{1}{2} b_1 \dot{\theta}_1 \cos \theta_2 + \frac{1}{3} b_2 (\dot{\theta}_1 + \dot{\theta}_2) \right) b_2^2 w / L \quad (7)$$

EOM of panel 1 is presented using maximal elevation angle (α_1) as:

$$I = \frac{1}{3} m_1 b_1^2 + \frac{1}{3} m_2 (b_1^2 + 3 b_1 b_2 \cos \theta_2 + 3 b_2^2) \quad (8)$$

$$T_s = -k_1(\theta_1 - \alpha_1) \quad \text{for bending step} \quad (9)$$

$$T_s = -k_1(-\theta_1) \quad \text{for flattening step} \quad (10)$$

$$T_{Drot} = \frac{1}{2} \rho \nu \left(\frac{1}{3} Z_d b_1 + Z_f b_2 \sin^2 \theta_2 \right) b_1^2 \dot{\theta}_1 w / L \quad (11)$$

Where w is the width of the panels, m_i , and b_i are the mass and the length, respectively, of panel- i , and θ_i , and k_i are the elevation angle and torsion spring constant, respectively, of spring- i .

The parameters for shape and density of the panels were determined from observation.

Significant bending and flattening motions were mostly completed within the order of several milliseconds or tens of milliseconds, and the fact that any significant damping vibration of crystals after bending or flattening was not observed indicated that k_i values were around 10^{-15} N m . Herein, we regarded that k_i ($i=1$ or 2) values were proportional to $1/b_i$ and w , referring to

the relationship between shear stress for a rectangular parallelepiped and Young's modulus by Equation 12.

$$k_i = E \frac{w d^3}{12 b_i} \quad (12)$$

Where E is a coefficient of stress/strain and d is the height of the rectangle.

For Type-A motion, we set α_2 as zero and alternated α_1 . For Type-B motion, α_2 and α_1 were changed subsequently, and θ_i was alternated to be constant or variable. For Type-C motion, α_1 and α_2 were alternated simultaneously, and θ_i was variable.

For translational motion, we regard that thrusts are generated by a sum of drag forces against fin rotation. Under this assumption, the acquired forces for horizontal translation by panels 1 and 2 (Th_1 , and Th_2 , respectively) are presented as Equations 13 and 14, and the drag force against translation (D_{transl}) is presented in Equation 15, in accordance with the equation for the drag force described in Equation 3.

$$Th_1 = \frac{1}{4} \rho v Z_d \dot{\theta}_1 b_1^2 w (-\sin \theta_1) / L \quad (13)$$

$$Th_2 = \frac{1}{2} \rho v Z_d \left(b_1 \dot{\theta}_1 \cos \theta_2 + b_2 (\dot{\theta}_1 + \dot{\theta}_2) \right) b_2 w (-\sin(\theta_1 + \theta_2)) / L +$$

$$\frac{1}{2} Z_f \rho v b_1^2 b_2 w \dot{\theta}_1 \sin \theta_2 \cos(\theta_1 + \theta_2) / L \quad (14)$$

$$D_{transl} = \frac{1}{2} \rho v (Z'_d S_d + Z'_f S_f) \dot{x} \quad (15)$$

Where Z' is the coefficient for the relationship between $1/Re$ and the drag coefficient to the shear face for translational motion. We regarded S_d as the projection area seen from the translational direction, and S_f as the area of projection seen from the vertical direction. Under this assumption, S_d and S_f are presented as

$$S_d = |b_1 \sin \theta_1 + b_2 \sin(\theta_1 + \theta_2)| w \quad (\text{while } \theta_1 + \theta_2 \geq 0)$$

$$S_d = |b_2 \sin(\theta_1 + \theta_2)| w \quad (\text{while } \theta_1 + \theta_2 < 0 \text{ and } b_1 \sin \theta_1 < b_2 \sin \theta_2)$$

$$S_d = |b_1 \sin \theta_1| w \quad (\text{while } \theta_1 + \theta_2 < 0 \text{ and } b_1 \sin \theta_1 \geq b_2 \sin \theta_2) \quad (16)$$

$$S_f = (b_0 + b_1 \cos \theta_1 + b_2 \cos(\theta_1 + \theta_2)) w \quad (17).$$

3. Results

Characterization of crystal swimming styles

As previously reported,^[12] the crystal showed self-continuous flipping under continuous irradiation by blue light through a sequence of time-irreversible processes, in which light-triggered isomerization of **1** (Steps 1 and 3, in Figure 2) induced a crystalline phase transition (Steps 2 and 4) which repeatedly progressed without external control. According to microscopic observation at several magnifications, the flipping direction was inherent in each crystal, and we suspect that the asymmetrical crystal outline and the asymmetrical crystal structure, the space group of which is expected to be P_1 ,^[15] determined the bending direction. Due to its limit-cycle mechanism with morphological change (Figure 2), the crystal stored the received energy and then sharply converted it to mechanical power. As a result, the crystal showed an intermittent swimming motion (Movie S1–S6). In other words, the crystal paddled itself forcefully with the intensive transformation at the phase transition steps (Steps 2 and 4) as shown in Figure 3. In our previous publication we reported that the maximum instantaneous speed was recorded precisely at the phase transition, the duration of which was less than ten milliseconds (Figure S3 in ref. 12), after which the crystal immediately ceased its translational motion. In contrast, photoisomerization-induced deformation of the crystal progressed slowly (steps 1 and 3), and offered less of an ability to propel itself.

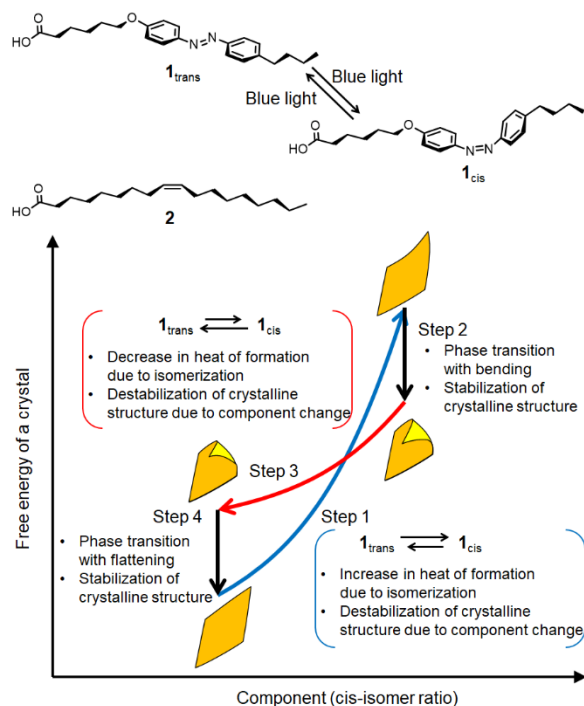


Figure 2. Schematic illustration of the energy cycle and explanation of each step for the limit-cycle transition of a self-oscillatory flipping crystal.

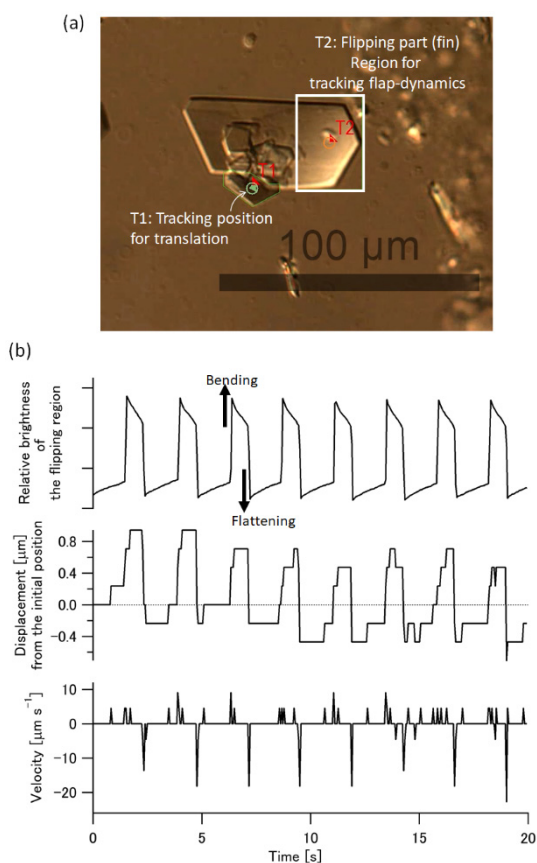


Figure 3. (a) Microscopic image of the crystal captured from Movie S3, which was recorded using a 19.3 fps camera. T1 and T2 indicate the location- and brightness-tracking points used to measure translational motion and fin flipping, respectively. (b) Changes in brightness, displacement, and speed of a self-flipping crystal over time, obtained from Movie S3. The sudden bending and flattening motions were completed in less than 50 ms.

Swimming efficiency depended on individual crystals (Figure 4). If the area and elevation angle of the flipped part (the “fin”) were larger, then the instantaneous speed was greater. Swimming direction also depended on individual crystals. Many crystals swam in a “stroke” style, with the fin in front (Movie S2); some swam with a “kicking” style in which the fin trailed behind (Movie S1); others swam in a “sidestroke” style, with the fin off to one side. The crystals that swam in a kicking style tended to lift their large, flat plane fins higher. However, this trend alone did not determine swimming style. Crystals swimming in the stroke style had various-sized fins and elevated them by various angles. In this study, the sidestroke swimmers were classified into either stroke or kicking style, depending on which way their orientation was biased.

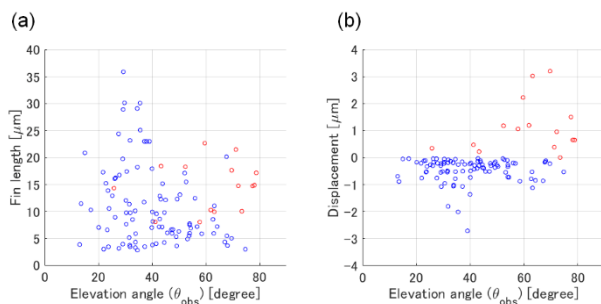


Figure 4. Distribution of swimming styles for the observed self-propelling crystals and their correlations between (a) fin length and elevation angle and (b) one-stroke displacement and elevation angle. The color red indicates that the crystal swam with a kicking style, the displacements of which are defined as positive values; the color blue indicates that the crystal swam with a stroke style, the displacements of which are defined as negative values.

Performance of the model

In this study, we used a three-linked-panel to model the bending crystal, because this is the simplest model for describing directional swimming motion of a plate-like object.^[18d] Table 1 shows the calculated results for the motion of an object with a total body length of 100 μm, each fin with a length (b_1 and b_2) of 10 μm, a width of 40 μm, and a height of 1 μm, under conditions of $E = 3 \times 10^3$ Pa and a maximum elevation angle (α) of 30°. Using these parameters, the observed elevation angles (θ_{obs}) were 30° for type-A, and 45° for Types-B1, -

B2, and -C motions. For Type-A, Type-B1 and Type-C motions, the object displayed a kicking motion; for Type-B2 it showed a stroke motion, a result of backward and forward translation within the bending and flattening processes, respectively. Figure 5 and Figure 6 illustrate the time course behavior of each model. The differences in fin endpoint trajectory when comparing bending and flattening routes illustrate that the object's motion is not completely reciprocal. The objects showed unidirectional swimming through an entire cycle of fin-flipping *in-silico* with the assumption that vertical motion of the main body was restricted.

Table 1. Calculated displacements of a three-panels-two-torsion springs model via Type-A, Type-B1, Type-B2, or Type-C one-round flipping motion.

Flipping motion	Swimming distance via single flipping / μm		
	Outbound	Inbound	Round
Type-A	-0.5	+ 3.0	+2.5 (kicking style)
Type-B1	-3.1	+4.6	+1.5 (kicking style)
Type-B2	-4.6	+ 3.1	-1.5 (stroke style)
Type C	-2.8	+ 4.5	+1.8 (kicking style)

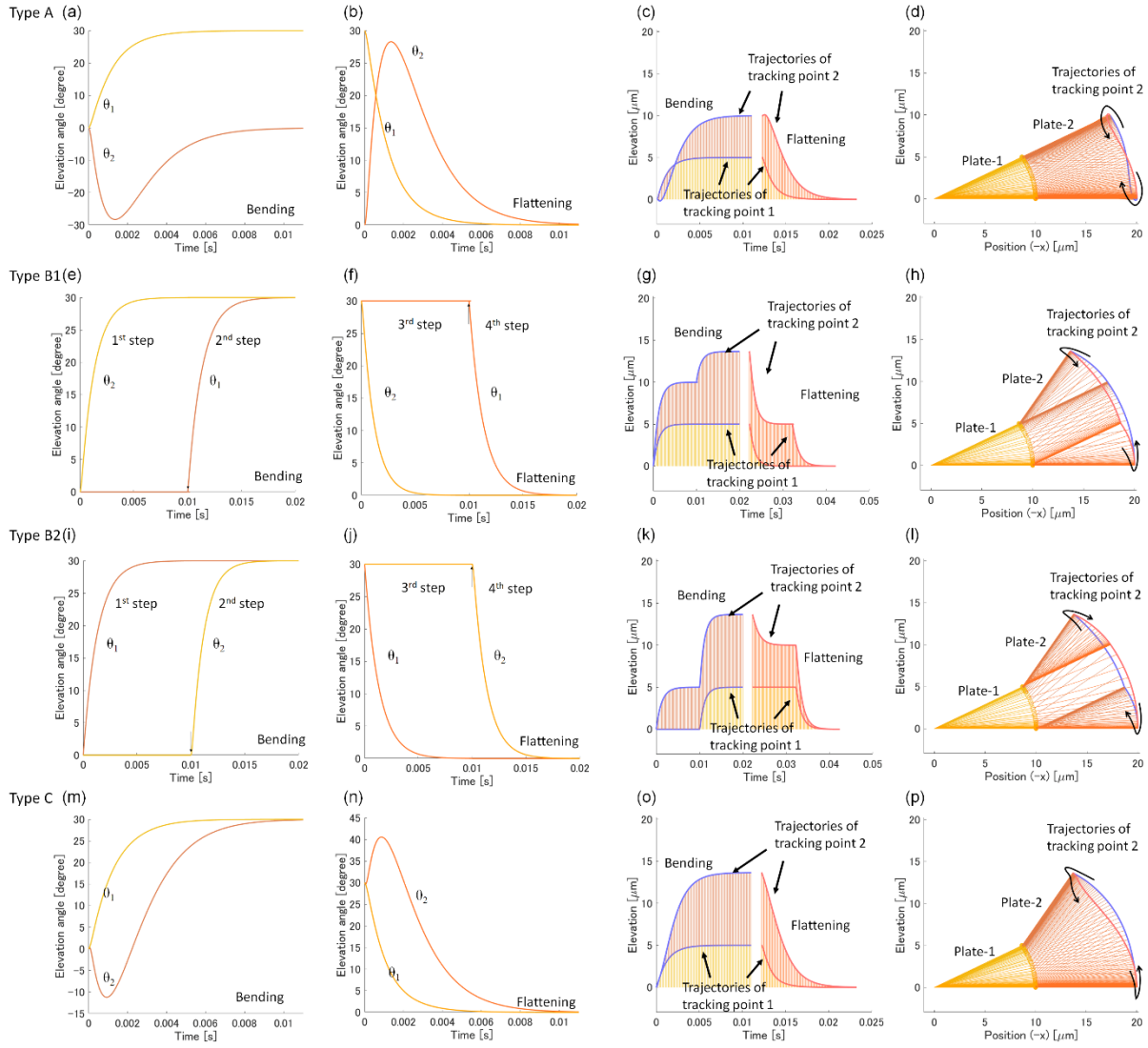


Figure 5. Examples of the rotational time-course behavior of panel-1 and panel-2 with 10 μm length each, calculated with Type-A (top), Type-B1 (middle-upper), Type-B2 (middle-lower), Type-C (bottom) motion using $E = 3 \times 10^3 \text{ Pa}$ and $\alpha = 30^\circ$. (a, e, i, m) show angular change of each panel during the bending motion. In Type-A and -C, the elevation angles for panel-2 (θ_2) decrease before they increase to the balanced angle, while the angle for panel-1 (θ_1) changes steadily to the balanced point. In Type-B1 and -B2, the orders of the panels' motion are fixed, and the angles change steadily to the balanced points in the order shown. (b, f, j, n) show angular change during the flattening motion. In Type-A and -C, the elevation angles for panel-2 (θ_2) increase before they decrease to the balanced angle, while the angles for panel-1 (θ_1) change steadily to the balanced point. In Type-B1 and -B2, the orders of the panels' motions are fixed, and the angles change steadily to the balanced points in the order shown. (c, g, k, o) show elevation attitude of the panel endpoints. Tracking point 1 corresponds to the position of spring-1 and tracking point 2 corresponds to the position of spring-2. (d, h, l, p) show a side view of the panels' motion throughout the entire time course. Together these results indicate that the trajectory of the panel-2 is not symmetrically reciprocal. The asymmetric motion can cause directional motion:^[20] see Figure 6.

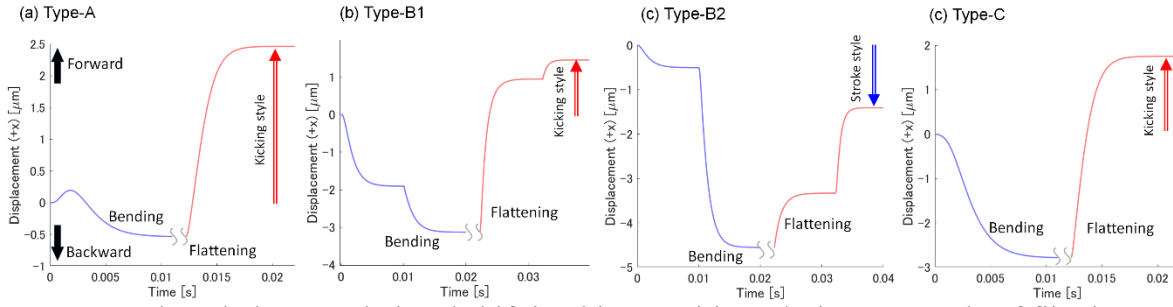


Figure 6. The relative translational shift in object positions during one cycle of flipping motion, calculated with (a) Type-A, (b) Type-B1, (c) Type-B2, and (d) Type-C motion, using the parameters $E = 3 \times 10^3$ Pa, $b_1 = b_2 = 10$ μm , and $\alpha = 30^\circ$. All the models describe backwards movement with the bending process, and forward movement with the flattening process. After a single cycle, Type-A, Type-B1, and Type-C experienced net forward movement, and Type B2 experienced net backwards movement.

We also solved the equations under various other conditions and calculated the displacements and values of forces and impulses for each. If each maximum elevation angle (α) was less than 60° , the Type-A and Type-B1 models resulted in a kicking-type motion, and the Type-B2 model resulted in a stroke-type motion, independent of fin-length. Hereafter we show only the results for Type-C motion which, like the actual crystals, showed both kicking-type and stroke-type motions.

Figure 7 shows contour plots for the estimated one-cycle flip displacements of an object with Type-C motion of the same size as the object shown above, calculated with variable fin-length ratio ($\text{FR} = b_2/(b_1+b_2) \times 100\%$) and elevation angles. Swimming styles shifted at $\text{FR} = 41\%$.

For larger FRs, the rotation of panel-2 delayed that of panel-1, and for smaller FRs the rotation of panel-1 delayed that of panel-2 (Figure 8). When FRs were near 41%, the angular velocities of panel-1 and panel-2 were similar to each other. In this case, the object behaved as a two-panel-one-torsion spring object and showed no net displacement, as predicted by the scallop theorem. The maximum displacement for kicking style was recorded as 3.1 μm at $\text{FR} = 59\%$ and $\alpha = 39^\circ$ ($\theta_{\text{obs}} = 62^\circ$), and the maximum displacement for stroke-style motion was recorded as 1.2 μm at $\text{FR} = 27\%$ and $\alpha = 40^\circ$ ($\theta_{\text{obs}} = 50^\circ$). The impulses calculated during bending and flattening for these conditions are shown in Table 2.

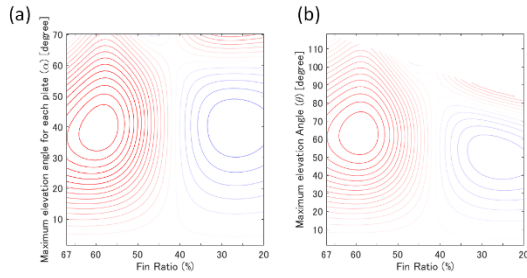


Figure 7. Contour plots to present the expected distribution of swimming styles and distances of a 20 μm fin-length flipping object with various elevation angles (α for (a) and θ for (b)) and with various fin ratios (FRs), calculated based on Type-C motion. Red indicates that the object showed kicking motion, while blue indicates that the object showed stroke-style motion. The intervals between the isobars indicate 0.2 μm .

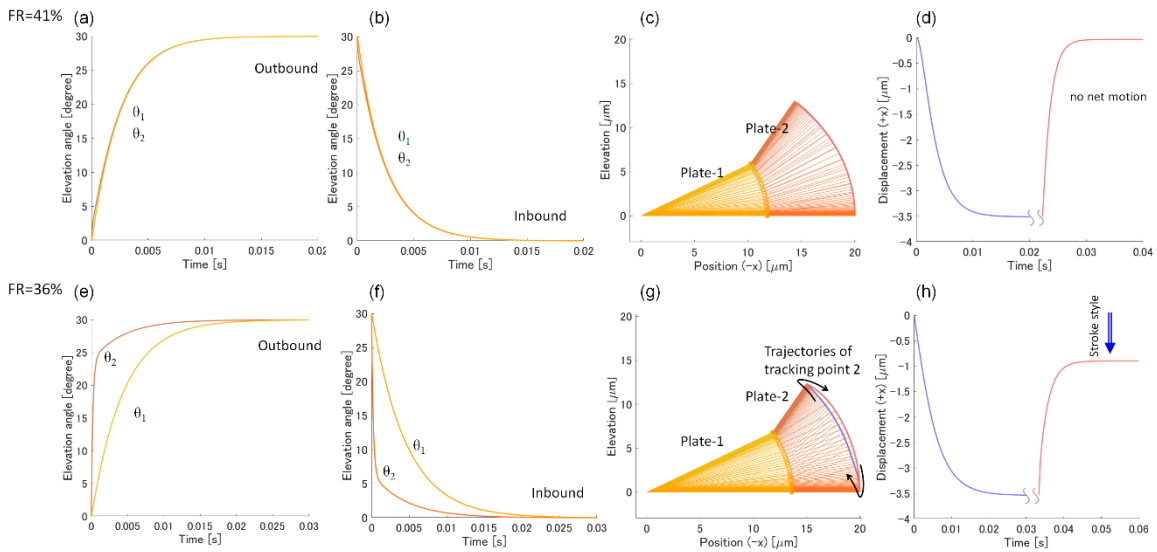


Figure 8. Rotational behavior of objects with fin-length ratios of 41% (upper) and 36% (lower) calculated with Type-C motion. (a, e) and (b, f) show the elevation angles over time while the panels undergo bending and flattening, respectively. (c, g) are side-views of panel-1 and panel-2 during a full cycle of flipping motion; (d, h) are the translational displacements calculated during a full cycle of the flipping motion. The model with a 41%-FR fin moves like a “two-panels” object, and does not show directional swimming. The model with a 36%-FR fin shows stroke-style swimming as shown in (h). In contrast to the result with 50%-FR model, the elevation angles for panel-2 (θ_2) achieves the balanced angle before panel-1 completes the rotational motion, as shown in (e, f). This leads to the breaking of symmetry in the trajectory of plate-2.

Table 2. Calculated impulses applied to the water according to the panels’ rotation

Fin ratio	Outbound (bending) process		Inbound (flattening) process	
	Impulse / N s	Horizontal component of impulse / N s	Impulse / N s	Horizontal component of impulse / N s
FR 50%	5.2×10^{-13}	1.6×10^{-13}	-5.0×10^{-13}	-2.6×10^{-13}
FR 41%	4.9×10^{-13}	2.0×10^{-13}	-4.9×10^{-13}	-2.0×10^{-13}
FR 36%	4.7×10^{-13}	2.1×10^{-13}	-4.7×10^{-13}	-1.7×10^{-13}

Figure 9 shows the results of model objects with variable fin lengths and elevation angles.

The fin length significantly affects the amplitude of displacement and the timescale of motion due to changes in the forces exerted by fin rotation. The value of E and thickness affected both the timescale and force strength of the rotation. However, the sum of impulses for a full cycle remained nearly constant as long as the fin did not show damping behavior. Changing the length of the main panel did not affect the rotational behavior of the other panels, but did slightly affect their translational behavior because of a change to the drag on the shear plane. Changing the width affected the strength of forces but did not change the pattern of motion.

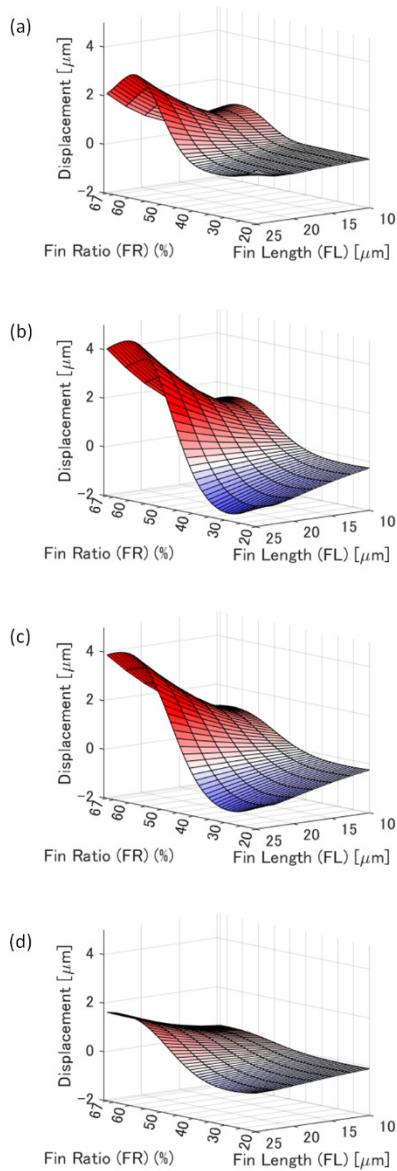


Figure 9. Displacement for one-flip motion of a panel calculated with variable fin length ($FL = b_1 + b_2$) and fin ratio ($FR = b_2/(b_1 + b_2)$) at various maximum elevation angles (α). (a) $\alpha = 60^\circ$, (b) $\alpha = 45^\circ$, (c) $\alpha = 30^\circ$, and (d) $\alpha = 15^\circ$.

4. Discussion

The bulk of our comparisons were between different FRs of panel-1 and panel-2. For panels of homogeneous physical properties, the lengths of the panels could be considered equal.

Under this assumption, panel-2 would receive a larger drag force to its rotational bending and flattening motion than panel-1. This circumstance would cause the rotation speed of panel-2 to slow, and the motion symmetry to break. As a result, as shown in Type-A, Type-B1, and Type-C motions, the object should show kicking-style swimming. Kicking-style swimming was indeed observed in several crystals. However, most of the crystals showed stroke-style swimming. In terms of the model, stroke style swimming occurs when the rotation of panel-2 precedes that of panel-1. This requirement is satisfied when the phase transition occurs subsequently from spring-2 to spring-1 as shown in Type-B2 motion, or when the FR is lower than 40% as in Type-C motion. In our observations of the crystals we were unable to distinguish whether the time delay in the phase transition existed; at least, we did not observe clear step-by-step rotations, as predicted in Figure 5. Furthermore, kicking-style swimming cannot be demonstrated by Type-B2 motion. From these considerations, we concluded that Type-C was the most probable for modeling the swimmers. However, it is not obvious what exactly is meant by panel-2 being shorter than panel-1. In the model, the three-linked panel accounts for the curved shape of the flapper. If the curvature was constant across the extent of the bending region, the lengths of b_1 and b_2 might be regarded as equal. However, considering that all of the stroke-style crystals had a thick stacked structure on the base side of the fin, we regarded the FR value as smaller than 50%, and only the model for Type-C motion could explain why so many crystals swam in this style. And the observation that kicking-style crystals had widely-extended planes and thin fins also supports this consideration.

Large displacement with kicking motion can be expected if the FR is larger than 50%, according to the Type-C model shown in Figure 7. However, it is not physically possible to achieve FRs larger than 50% because this would entail the body-side fin being more flexible than the edge-side fin. Figure 10 shows the expected trend between elevation angle and one-flip displacement for crystals with $FR \leq 50\%$. The peak angle is expected to be lower for the stroke style than for the kicking style. The fact that the expected trend is in good agreement with the observed result shown in Figure 4b indicates that type-C motion simulated well the behavior of the crystalline swimmer, although the possibility of a more detailed discussion is limited due to variations in the crystal outlines. It should be noted that the calculated displacement was somewhat smaller than the observed maximum value, possibly due to an overestimation of b_0 and S_d .

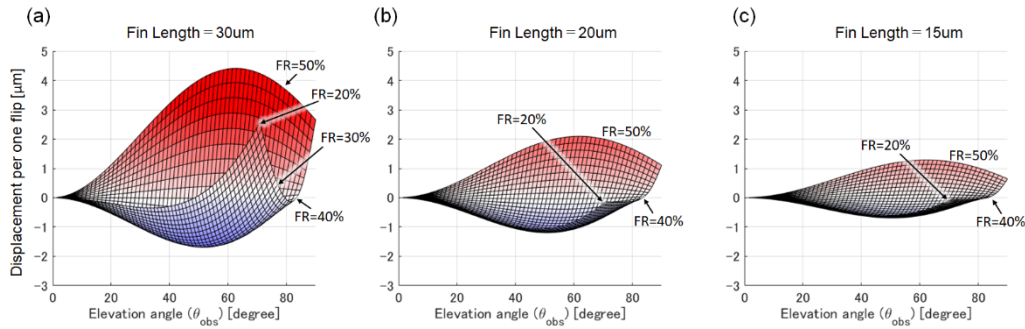


Figure 10. Calculated displacements for a one-flip motion of the panel with variable elevation angles (θ_{obs}) and variable FR ($20\% \leq FR \leq 50\%$). The fin length of the model object was (a) 30 μm , (b) 20 μm , and (c) 15 μm .

The mechanical properties of the motion were estimated based on the Type-C model, which showed good fit despite our choosing to ignore some of the complexities of hydrodynamics. Impulses to the external fluid for half-rotations (under conditions of $\alpha = 30^\circ$ and $FR = 50\%$) were estimated to be around $5 \times 10^{-13} \text{ N s}$ due to the accumulation of drag forces and their horizontal components (31% and 52% for bending and flattening, respectively) being transferred to the translational momentum of water flow via inelastic collision. Thus, crystalline rotation leads to translational motion of the water and drag forces acting on the

fins, which in turn leads to crystalline translation, the kinetic energy of which is immediately and completely dissipated to the surroundings. Even given a larger spring constant, the impulse used for swimming would be the same unless the crystal's shape or deformation style changes. Such mechanics and low efficiency are not unexpected for an object that swims at a low Reynolds number.

In summary, both experimental observation and simplified modeling demonstrated that a self-sustainable bending crystal can swim directionally in a two-dimensional tank. However, the near-reversible flipping motion does not result in swimming with high efficiency. A more efficient motion would be expected from an object that rotates with a large symmetry break, such as in microorganisms that move with a flagellar spiral motion. However, there is a trade-off between the assembled structure of molecules and freedom of movement. Three-dimensional objects have no freedom of motion. On the other hand, two-dimensional objects can perform flip or wave-like motions and swim autonomously, albeit with low efficiency. A one-dimensional assembly may show spiral motion and be an efficient swimmer, but such macroscopic autonomous motion has not yet been synthetically created. Overall, this study shows a basic design for the creation of small, artificial active motion devices.

Supporting Information

Supporting Information (Movie S1–S6 and Figure S1 and S2) is available from the Wiley Online Library.

Acknowledgements

Y. K. thanks Dr. Takuji Nakashima (Hiroshima Univ.) for his kind suggestions. Y. K. and K. O. thank Prof. Hideo Kubo (Hokkaido Univ.) for his introductive training for mathematical analysis. The research was supported by JSPS KAKENHI Grant Number JP18H05423 in Scientific Research on Innovative Areas "Molecular Engine" and JP20H04622 in Scientific Research on Innovative Areas "Discrete Geometric Analysis for Materials Design". K.O. was supported by MEXT through the Program for Leading Graduate Schools (Hokkaido University "Ambitious Leader's Program").

Conflict of Interest

All authors have no conflicts of interest.

Received: ((will be filled in by the editorial staff))

Revised: ((will be filled in by the editorial staff))

Published online: ((will be filled in by the editorial staff))

References

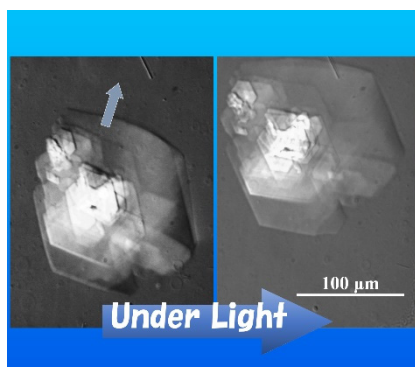
- [1] a) R. Feynman, *J. Microelectromechanical Syst.* **1993**, 2, 4-14; b) S. Sánchez, L. Soler, J. Katuri, *Angew. Chem. Int. Ed.* **2015**, 54, 1414-1444; c) R. Salazar, V. Fuentes, A. Abdelkefi, *Ocean Eng.* **2018**, 148, 75-114; d) H. Zeng, P. Wasylczyk, D. S. Wiersma, A. Priimagi, *Adv. Mater.* **2018**, 30, e1703554; e) S. Palagi, D. P. Singh, P. Fischer, *Adv. Opt. Mater.* **2019**, 7, 1900370.
- [2] a) M. Camacho-Lopez, H. Finkelmann, P. Palffy-Muhoray, M. Shelley, *Nat. Mater.* **2004**, 3, 307-310; b) Y. S. Kim, M. Liu, Y. Ishida, Y. Ebina, M. Osada, T. Sasaki, T. Hikima, M. Takata, T. Aida, *Nat. Mater.* **2015**, 14, 1002-1007; c) H. Arazoe, D. Miyajima, K. Akaike, F. Araoka, E. Sato, T. Hikima, M. Kawamoto, T. Aida, *Nat. Mater.* **2016**, 15, 1084-1089; d) R. Piotrowska, T. Hesketh, H. Wang, A. R. G. Martin, D. Bowering, C. Zhang, C. T. Hu, S. A. McPhee, T. Wang, Y. Park, P. Singla, T. McGlone, A. Florence, T. Tuttle, R. V. Ulijn, X. Chen, *Nat. Mater.* **2021**, 20, 403-409; e) S. Gangwal, O. J. Cayre, M. Z. Bazant, O. D. Velev, *Phys. Rev. Lett.* **2008**, 100, 058302.
- [3] a) S. Palagi, A. G. Mark, S. Y. Reigh, K. Melde, T. Qiu, H. Zeng, C. Parmeggiani, D. Martella, A. Sanchez-Castillo, N. Kapernaum, F. Giesselmann, D. S. Wiersma, E. Lauga, P. Fischer, *Nat. Mater.* **2016**, 15, 647; b) M. Rogó , H. Zeng, C. Xuan, D. S. Wiersma, P. Wasylczyk, *Adv. Opt. Mater.* **2016**, 4, 1689-1694; c) Z.-C. Jiang, Y.-Y. Xiao, X. Tong, Y. Zhao, *Angew. Chem. Int. Ed.* **2019**, 58, 5332-5337; d) H. Zeng, P. Wasylczyk, C. Parmeggiani, D. Martella, M. Burrelli, D. S. Wiersma, *Adv. Mater.* **2015**, 27, 3883-3887; e) C. Huang, J.-a. Lv, X. Tian, Y. Wang, Y. Yu, J. Liu, *Sci. Rep.* **2015**, 5, 17414.
- [4] Z. Sun, Y. Yamauchi, F. Araoka, Y. S. Kim, J. Bergueiro, Y. Ishida, Y. Ebina, T. Sasaki, T. Hikima, T. Aida, *Angew. Chem. Int. Ed.* **2018**, 57, 15772-15776.
- [5] a) H. Cui, Q. Zhao, Y. Wang, X. Du, *Chem. Asian J.* **2019**, 14, 2369-2387; b) X. X. Le, W. Lu, J. W. Zhang, T. Chen, *Adv. Sci.* **2019**, 6; c) M. C. Koetting, J. T. Peters, S. D. Steichen, N. A. Peppas, *Mater. Sci. Eng. R: Reports* **2015**, 93, 1-49; d) A. Harada, Y. Takashima, M. Nakahata, *Acc. Chem. Res.* **2014**, 47, 2128-2140; e) F. D. Jochum, P. Theato, *Chem. Soc. Rev.* **2013**, 42, 7468-7483; f) A. S. Hoffman, *Adv. Drug Deliv. Rev.* **2013**, 65, 10-16; g) A. Doring, W. Birnbaum, D. Kuckling, *Chem. Soc. Rev.* **2013**, 42, 7391-7420; h) B. Rybtchinski, *ACS Nano* **2011**, 5, 6791-6818.
- [6] a) Y. Kageyama, *ChemPhotoChem* **2019**, 3, 327-336; b) J. Parmar, D. Vilela, K. Villa, J. Wang, S. Sánchez, *J. Am. Chem. Soc.* **2018**, 140, 9317-9331.
- [7] a) S. Du, H. Wang, C. Zhou, W. Wang, Z. Zhang, *J. Am. Chem. Soc.* **2020**, 142, 2213-2217; b) H.-R. Jiang, N. Yoshinaga, M. Sano, *Phys. Rev. Lett.* **2010**, 105, 268302; c) W. F. Paxton, K. C. Kistler, C. C. Olmeda, A. Sen, S. K. St. Angelo, Y. Cao, T. E. Mallouk, P. E. Lammert, V. H. Crespi, *J. Am. Chem. Soc.* **2004**, 126, 13424-13431; d) J. Shao, S. Cao, D. S. Williams, L. K. E. A. Abdelmohsen, J. C. M. van Hest, *Angew. Chem. Int. Ed.* **2020**, 59, 16918-16925; e) H. Lv, Y. Xing, X. Du, T. Xu, X. Zhang, *Soft Matter* **2020**, 16, 4961-4968; f) R. M. Hormigos, B. J. Sánchez, A. Escarpa, *Angew. Chem. Int. Ed.* **2019**, 58, 3128-3132.
- [8] a) T. Ban, T. Yamagami, H. Nakata, Y. Okano, *Langmuir* **2013**, 29, 2554-2561; b) T. Banno, A. Asami, N. Ueno, H. Kitahata, Y. Koyano, K. Asakura, T. Toyota, *Sci. Rep.*

- 2016**, 6, 31292; c) M. Schmitt, H. Stark, *Phys. Fluid.* **2016**, 28; d) N. J. Suematsu, K. Saikusa, T. Nagata, S. Izumi, *Langmuir* **2019**, 35, 11601-11607; e) F. Takabatake, N. Magome, M. Ichikawa, K. Yoshikawa, *J. Chem. Phys.* **2011**, 134, 114704.
- [9] S. Maeda, Y. Hara, T. Sakai, R. Yoshida, S. Hashimoto, *Adv. Mater.* **2007**, 19, 3480-3484.
- [10] a) A. H. Gelebart, D. Jan Mulder, M. Varga, A. Konya, G. Vantomme, E. W. Meijer, R. L. B. Selinger, D. J. Broer, *Nature* **2017**, 546, 632-636; b) H. Nakano, M. Suzuki, *J. Mater. Chem.* **2012**, 22, 3702-3704; c) E. Uchida, R. Azumi, Y. Norikane, *Nat. Commun.* **2015**, 6, 7310.
- [11] Y. Kageyama, *Symmetry* **2020**, 12, 1688.
- [12] T. Ikegami, Y. Kageyama, K. Obara, S. Takeda, *Angew. Chem. Int. Ed.* **2016**, 55, 8239-8243.
- [13] a) Y. Kageyama, N. Tanigake, Y. Kurokome, S. Iwaki, S. Takeda, K. Suzuki, T. Sugawara, *Chem. Commun.* **2013**, 49, 9386-9388; b) Y. Kageyama, T. Ikegami, Y. Kurokome, S. Takeda, *Chem. Eur. J.* **2016**, 22, 8669-8675.
- [14] As previously reported in ref.15, the preparation of the co-crystal of **1** and **2** is easier than that of the single component self-oscillatory crystal of **1**. It is speculated that the co-crystal is the crystal that the two-of-six azobenzenes of the single component crystal are substituted.
- [15] Y. Kageyama, T. Ikegami, S. Satonaga, K. Obara, H. Sato, S. Takeda, *Chem. Eur. J.* **2020**, 26, 10759-10768.
- [16] E. Lauga, *Soft Matter* **2011**, 7, 3060-3065.
- [17] E. M. Purcell, *Proc. Nat'l. Acad. Sci. USA* **1997**, 94, 11307-11311.
- [18] a) D. Gonzalez-Rodriguez, E. Lauga, *J. Phys. Condens. Matter* **2009**, 21, 204103; b) R. Golestanian, A. Ajdari, *Phys. Rev. E* **2008**, 77, 036308; c) M. Tarama, T. Ohta, *Europhys. Lett.* **2016**, 114, 30002; d) L. E. Becker, S. A. Koehler, H. A. Stone, *J. Fluid Mech.* **2003**, 490, 15-35.
- [19] A. Azuma, Seibutsuno Ugokino Jiten, Asakura Shoten, Shinjuku Tokyo, Japan 2018.
- [20] M. Lahikainen, H. Zeng, A. Priimagi, *Soft Matter* **2020**, 16, 5951-5958.

Self-propulsion of a light-powered microscopic crystalline flapper in water

Kazuma Obara, Yoshiyuki Kageyama,* Sadamu Takeda

Self-propulsion of a submillimeter-sized crystal of molecular motor in a water pool is realized under continuous-wave visible light irradiation. The crystal drives itself by self-oscillatory reciprocal flapping motion. Whether the swimmer excels at the stroking or kicking style is governed by slight differences in the outline of the crystals.



Supporting Information

Self-propulsion of a light-powered microscopic crystalline flapper in water

Kazuma Obara, Yoshiyuki Kageyama, and Sadamu Takeda*

Movie S1.

Stroke-style self-propulsion of crystals.

Movie S2.

Kicking-style self-propulsion of crystals.

Movie S3.

Back-and-force motion of a crystal analyzed in Figure 3.

Movie S4.

Comparison of the swimming crystals with similar outlines, the motion was analyzed in Figure S2 in the supporting information.

Movie S5.

Self-oscillatory motion of crystals, observed using objective lenses with 20× and 10× magnification.

Movie S6.

Stroke-style swimming of a crystal under various intensities of light.

Figure S1.

Illustration for the observation system.

Figure S2.

Comparison of the swimming of two crystals with similar outlines.

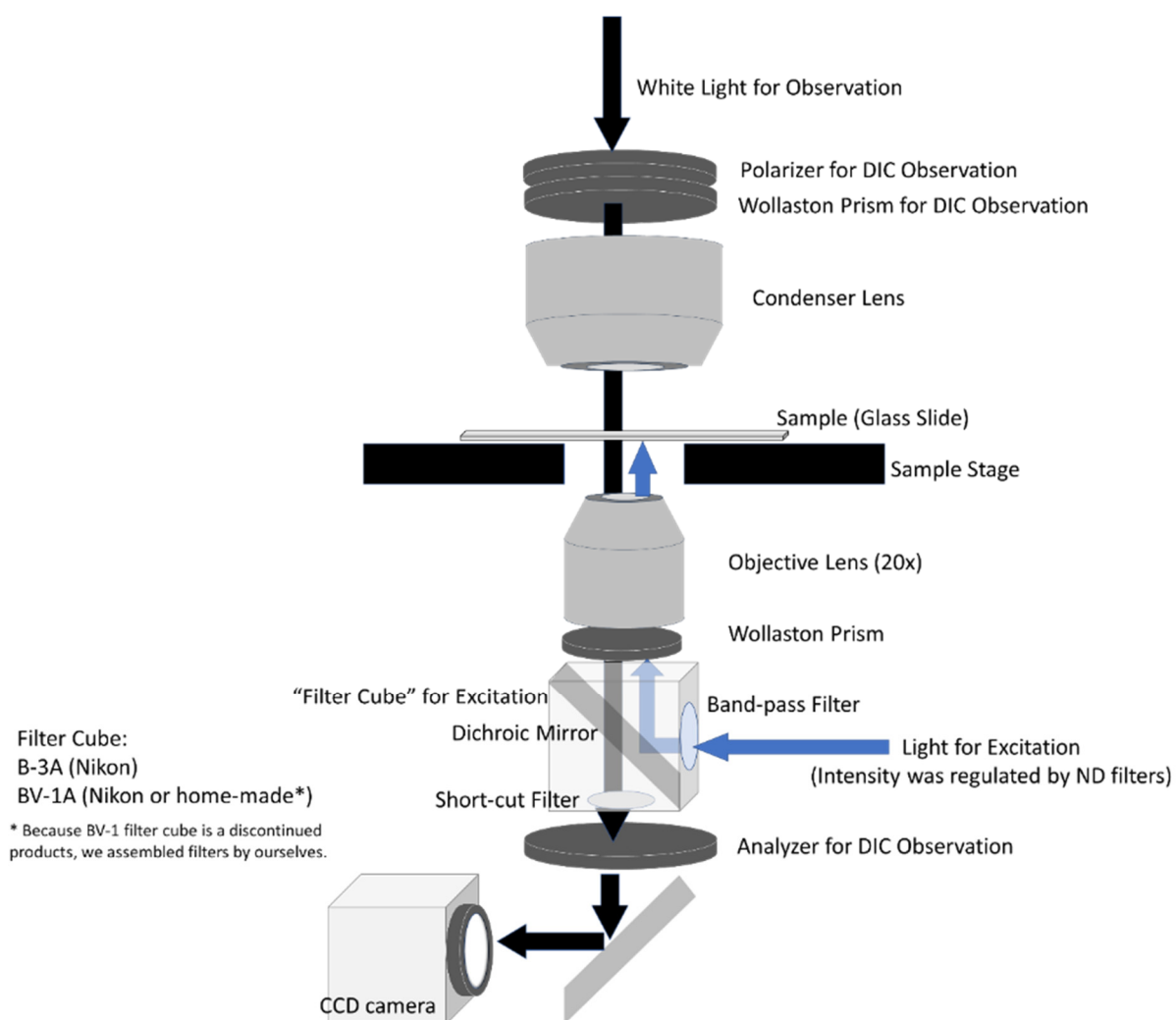


Figure S1. Illustration of the observation system.

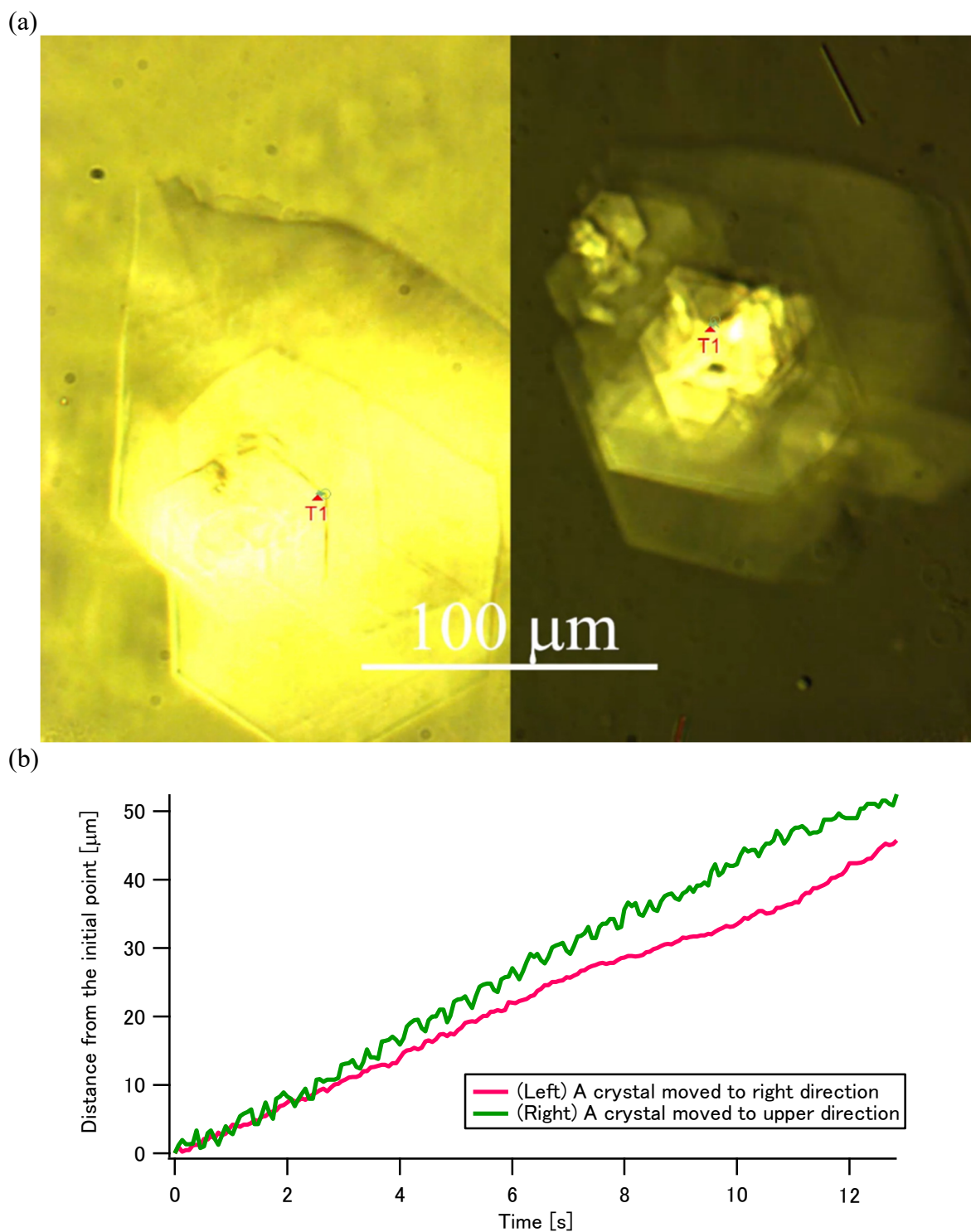


Figure S2. Comparison of stroke-style crystal swimmers with similar size. (a) A captured image for two crystal swimmers from Movie S4. (b) Swimming distances from the initial position of the swimmers. Magenta line is for the left crystal, and green line is for the right crystal. The movie was recorded at 15.5 fps, using a 20 \times objective lens and a B-3A filter cube (Nikon, Japan).